Design of a Single-Stage Inductive-Power-Transfer Converter for Efficient EV Battery Charging

Zhicong Huang, *Student Member, IEEE*, Siu-Chung Wong, *Senior Member, IEEE*, and Chi K. Tse, *Fellow, IEEE*

***Abstract*—This paper studies wireless charging of lithium-ion batteries for electric vehicles. The charging profile mandates a constant-current (CC) charging for a discharged battery until the battery voltage reaches the cutoff voltage at rated power. The charging continues at the cutoff voltage with a constant-voltage (CV) charging at a power level down to 3% of the rated power in order to fully charge the battery. An inductive-power-transfer (IPT) converter should be designed with minimal number of stages to achieve high efficiency. However, high efficiency for such a wide load range is difficult to achieve. Moreover, the efficiency-to-load relationship is distinctly different for CC and CV charging operations, posing difficulties for the single-stage design. This paper describes the design of a single-stage IPT converter that complies with the battery charging profile and, at the same time, achieves optimal efficiency. Design optimization includes soft switching for the entire battery load range, efficiency optimization for CC and CV modes of operation, and system efficiency optimization for the whole battery charging profile. Measured results of two experimental IPT battery chargers are presented for illustration and verification.**

***Index Terms*—Battery charger, electric vehicles (EVs), system efficiency, wireless power transfer.**

I. Introduction

The direct burning of fossil fuels in combustion engines of vehicles incurs increasing financial and environmental costs. In recent years, demand for green electric vehicles (EVs) has grown significantly. First generation of EVs uses predominantly simple plug-in charging methods, which have safety issues caused by exposed plugs and damaged cables. To eliminate plugs and cables, wireless charging methods have been widely studied [1]–[4]. A wireless charging system can have both the primary and secondary sides fully insulated and without physical contact. Thus, it is versatile in humid and adverse weather conditions. The charging process can be designed to be automatic, safe, and user convenient.

Wireless EV battery charging usually uses a loosely coupled transformer in an inductive-power-transfer (IPT) process to convert power from the primary side to the secondary side separated by a large predefined air gap [5], [6]. Compensation using external reactive elements to form resonant tank circuits is often required for both primary and secondary windings of the transformer to enhance the power transfer capability, to minimize the VA rating of the power supply, to regulate separately the currents in the supply loop and the receiving loop, and to achieve a higher efficiency. Studies have been carried out for selecting the most appropriate compensation topology for IPT systems for specific applications [2], [7]–[12].

Lithium-ion (Li-ion) batteries are widely used in EVs. The charging process for Li-ion batteries usually consists of four main stages [13], [14]: trickle charging, constant-current (CC) charging, constant-voltage (CV) charging, and charge termination. A CC charging stage followed by a CV charging stage is the preferred charging algorithm for Li-ion batteries. The charging current at the CC stage does not need to be precise and a quasi-CC is allowed [15]. With this charging algorithm, a converter should charge a load with power varying from the maximum rated power down to a minimum of about 3%. This efficiency optimization requirement is challenging for most converter topologies.

An IPT power converter is, in general, a resonant converter, which consists of an inverter driving a resonant circuit. An ideal inverter circuit can have the highest efficiency when it is driving a pure resistive load. Therefore, the resonant circuit is mostly designed with zero-phase angle (ZPA) at the operating frequency driven by the inverter switches, where the inverter switches can operate at both zero-voltage and zero-current switching [11]. However, application of different power switches may need to have a slight different adjustment. The popular MOSFET power switches have significant parasitic drain-to-source capacitances. The resonant circuit is, thus, designed slightly inductive to absolve all the charges of the capacitances of the inverter switches before the instance of active turning on (soft switching). Since the resonant circuit is slightly inductive, the switches have to be turned ON at zero-voltage [zero-voltage switching (ZVS)]. The corresponding currents at switching instance are not zero and need to be kept small to reduce conduction loss during the transition of turning ON. It is noted that the depth of direct modulation of the inverter switches should be kept shallow to maintain good efficiency of soft switching. The reasons are that for pulse width modulation (PWM), the soft switching is difficult to maintain, and for frequency modulation (FM), the conduction losses during switching instance at higher operation frequency can be significant.

The soft switching IPT converters can further achieve optimal efficiency at some resonant frequencies with matched input and

Manuscript received July 21, 2016; revised October 24, 2016; accepted November 14, 2016. Date of publication November 22, 2016; date of current version July 14, 2017. This work was supported by Hong Kong Polytechnic University under Central Research Grant G-YBKC. The review of this paper was coordinated by Dr. B. Akin.

The authors are with the Department of Electronic and Information Engineering, The Hong Kong Polytechnic University, Hong Kong (e-mail: zhicong.huang@connect.polyu.hk; enscwong@polyu.edu.hk; encktse@polyu.edu.hk).

Color versions of one or more of the figures in this paper are available online at http://ieeexplore.ieee.org.

Digital Object Identifier 10.1109/TVT.2016.2631596

output impedances. Deviating from this optimal matching point, the converter efficiency suffers [16]. In view of the narrow input impedance and output impedance ranges of resonant converters, multistage converter topologies with input and/or output power converters connected in-front-of and/or after the IPT converter have been proposed [17]–[19], hoping to improve system efficiency by operating the resonant converter without modulation at its optimal load while allowing losses of extra efficient converters. The obvious drawbacks of these multistage converters are the following.

1) More converters are used.
2) More complicated control may be needed for the coordination of controls between the primary and secondary sides of the IPT converter.
3) These topologies are for general applications as they are designed for an arbitrary variation of load range without optimizing the power loss and the charging time of the battery charging profile.

Without the additional cascaded power converter(s) for the tracking of the input and/or load impedance, a single-stage IPT converter has less degree of freedom for optimization under the specific charging profile. The single-stage IPT converter can be designed for maximum efficiency at maximum load power. Thus, the IPT converter can efficiently operate with shallow modulation at either its load-independent voltage (LIV) output operation point using series–parallel (S-P) compensation or load-independent current (LIC) output operation point using series–series (S-S) compensation [11], [12]. At these operation points, the equivalent reactance on the inverter switches is near ZPA. To achieve energy-efficient CC and CV charging stages with narrow-range PWM control and/or FM control, switching of IPT compensation topologies from S-S compensation to S-P compensation is needed [20]. These hybrid- or dual-topology IPT converters necessitate extra power switches along the main power path of the converter, incurring additional cost for power switches and power loss. Meanwhile, the CV converter is still required to charge the battery load with power varying from the full rated power to a minimum of about 3% of the rated power.

In Section II, the conditions for LIC output and LIV output of the single-stage S-S compensated IPT (SSIPT) converter at two different operating frequencies for CC charging and CV charging stages of the EV battery are first reviewed. The efficiency of the SSIPT converter topology is then analyzed in terms of the quality factor of Litz-wire windings. Since the system is operating at two fixed frequencies within the full range of an EV battery charging profile, the proposed EV battery charging method will simplify the control design and improve reliability. A nominal load quality factor Q_n during the transition from CC to CV operation is determined by optimizing the overall system efficiency of the converter for the entire charging profile in Section III. The analytical results are experimentally evaluated in Section IV. Finally, Section V concludes the paper.

II. Characteristics of the SSIPT System

The SSIPT converter has been extensively studied [7], [8], [10]–[12], [17]–[23]. To eliminate the power loss associated with the multistage and hybrid-topology IPT converter at rated power, some design options for a single-topology IPT converter are available. First, the single-topology IPT converter can operate near its maximal efficiency point and be controlled for the required two stages of battery charging. Alternatively, it may operate at its optimal efficiency point for the first stage of CC or second stage of CV charging and use a control technique with reduced efficiency for the other stages of charging. Furthermore, it may operate at its optimal efficiency points at LIC and LIV for the first and second stages of charging, respectively. The possible cases of implementations for a single-topology IPT converter are summarized in Table I.

TABLE I
Cases of Implementation

Case	Operating point	CC charging	CV charging
(C1)	LIV	MC	MC
(C2)	LIC	MC	MC
(C3)	LIV	MC	native
(C4)	LIC	native	MC
(C5)	LIC	native	
	LIV		native

note: MC—modulation and control
native — minimal modulation for efficiency

In Table I, cases (C1) and (C2) are mostly achieved by utilizing different depth and type of modulations. Without modulation, the converter can be efficiently operated at operation points LIV and LIC. As a rule of thumb, efficiency suffers from more depth of modulation.

Case (C1) has been used in a SSIPT converter with a simple narrow-frequency-range FM control [21]. Normally, a frequency limiter is used to implement the FM control [21] to maintain stability in the loosely coupled systems [21], [24], [25]. It is obvious that the single-topology SSIPT converter operating near the LIV operating point [21] can only be optimized for efficiency with an operating frequency at a single loading point for the CC and CV modes of charging for an EV battery. Likewise, this also applies to case (C2). However, due to their operations near LIC operating point, cases (C2) and (C4) require deep modulation to satisfy the wide current range within the CV charging stage of the battery charging profile. Thus, a large variation of the phase angle between the driving voltage and the current of a compensated IPT transformer is needed, making soft switching impossible if FM or PWM control is employed for the required load range [26]. In contrast, an IPT converter operating at its resonance, i.e., SSIPT converter operating at LIC operating point, is found to be most power efficient [7], [10], [17]–[19], [22], making implementation of case (C3) less attractive than case (C5).

In this paper, a single-stage SSIPT converter operating at LIC for CC charging and at LIV for CV charging complying with an EV battery profile [i.e., case (C5)] is designed and optimized for efficiency and ease of control. The LIC operating point of the SSIPT converter can provide maximum efficiency at rated power for charging a significant part of the charging profile, while the LIV operation point of the SSIPT converter can eliminate the loss due to control during CV charging of the

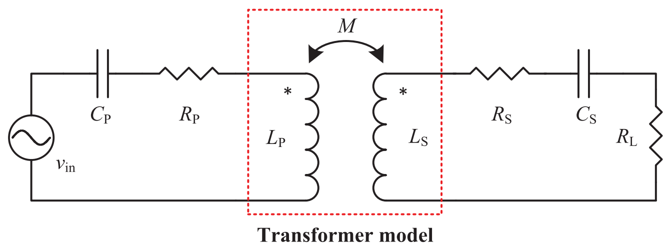

Fig. 1. S-S compensated IPT topology.

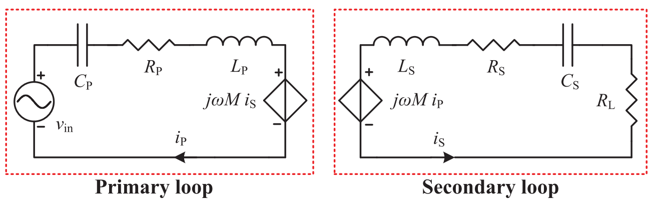

Fig. 2. Equivalent circuit model of Fig. 1.

EV battery. A minimal amount of control is needed as the LIC and LIV operations naturally provide the required CC and CV outputs, respectively.

In this section, we highlight the LIC and LIV transfer characteristics of the SSIPT converter and analyze the efficiency of the converter during LIC and LIV operations. The model used ignores the switching loss due to the transistor parasitic capacitor, finite rise time, and finite fall time. The practical efficiency degradation will be discussed in Section IV.

A. Circuit Topology and Equivalent Circuit Model

The commonly used loosely coupled transformer model, as shown in Fig. 1, for the SSIPT converter is adopted in this paper [11], [12], [23]. Transformer inductances L_P in the primary side, L_S in the secondary side, and mutual inductance M are components of the transformer model shown in Fig. 1. In the circuit model, R_P and R_S are the winding resistances of the transformer primary and secondary, respectively. Also, C_P and C_S are the primary and secondary external compensation capacitors for enhancing energy transfer from an ac source v_{in} to an output loading resistance R_L. The ac source is generally taken as an equivalent voltage generated from a half-bridge or full-bridge switching circuit operating at an angular frequency ω.

As usual, a frequency-domain equivalent circuit is adopted and only the fundamental component is considered here for simplicity [3], [11], [12], [23], [24]. Discrepancies in practical applications will be discussed in Section IV.

Without introducing ambiguity, voltage and current valuables are considered as phasors for subsequent analyses. Fig. 2 shows an equivalent circuit of Fig. 1 for steady-state analysis. The dependent source $j\omega M i_S$ in Fig. 2 can be replaced by Z_r, which is an equivalent impedance reflected from the secondary side to the primary side. Thus, the primary loop is decoupled from the secondary loop [11].

B. Ideal Transconductance and Voltage Transfer Ratio

We summarize the basic analysis of an SSIPT converter in this subsection [11], [12]. The output current i_o and output voltage v_o are calculated with the parameters given in Table II. The ratio of output current i_o and input voltage v_{in} is defined as transconductance G, i.e.,

TABLE II
PARAMETERS FOR CALCULATION

Z_S	$j\omega L_S + \frac{1}{j\omega C_S} + R_S + R_L$
Z_P	$j\omega L_P + \frac{1}{j\omega C_P} + R_P$
Z_r	$\frac{\omega^2 M^2}{Z_S}$
i_P	$\frac{v_{\text{in}}}{Z_P + Z_r}$
i_o	$\frac{j\omega M i_P}{Z_S}$
v_o	$i_o R_L$

$$G(\omega) = \frac{i_o}{v_{\text{in}}} = \frac{j\omega M}{Z_P Z_S + \omega^2 M^2}. \tag{1}$$

The ratio of output voltage v_o and input voltage v_{in} is defined as the voltage transfer ratio, E, i.e.,

$$E(\omega) = \frac{v_o}{v_{\text{in}}} = \frac{j\omega M R_L}{Z_P Z_S + \omega^2 M^2}. \tag{2}$$

The primary resonant angular frequency ω_P and the secondary resonant angular frequency ω_S are defined as

$$\omega_P = \frac{1}{\sqrt{L_P C_P}} \text{ and } \omega_S = \frac{1}{\sqrt{L_S C_S}}. \tag{3}$$

In previous applications, their ratio

$$\mu = \frac{\omega_P}{\omega_S} \tag{4}$$

is normally set at unity by choosing external compensation capacitors C_P and C_S, i.e., $\omega_P = \omega_S$. We will show in Section II-E that a nonunity μ is necessary to achieve soft switching of the main switches during CC mode of operation.

The characteristics of ideal transconductance and ideal voltage transfer ratio, denoted as G_i and E_i, respectively, are obtained by assuming $R_P = R_S = 0$. Transfer functions G_i and E_i can be load independent at some operating frequencies. The frequencies can be found by setting the coefficients of R_L in (1) and (2) to zero [27]. The load-independent transconductance G_i can operate at ω_P and its magnitude is determined as

$$|G_i(\omega_P)| = \frac{1}{\omega_P k\sqrt{L_P L_S}}. \tag{5}$$

Note that μ should be designed close to 1, i.e., $\omega_P \approx \omega_S$. Otherwise, the converter efficiency described in Section II-C might suffer. Likewise, LIV ratio E_i is given by

$$|E_i(\omega_L)| = \sqrt{\frac{L_S}{L_P}}\left|\frac{k(\mu^2 + 1 - \Delta)}{(2k^2 - 1)\mu^2 + 1 - \Delta}\right| \tag{6}$$

$$|E_i(\omega_H)| = \sqrt{\frac{L_S}{L_P}}\left|\frac{k(\mu^2 + 1 + \Delta)}{(2k^2 - 1)\mu^2 + 1 + \Delta}\right| \tag{7}$$

where $\Delta = \sqrt{(1-\mu^2)^2 + 4k^2\mu^2}$, and the operating angular frequencies are given by

$$\omega_L = \omega_S \sqrt{\frac{\mu^2 + 1 - \Delta}{2(1-k^2)}} \tag{8}$$

$$\omega_H = \omega_S \sqrt{\frac{\mu^2 + 1 + \Delta}{2(1-k^2)}}. \tag{9}$$

Hence, the SSIPT converter has an LIC output of $|G_i(\omega_P)|$ suitable for CC charging and a LIV output of $|E_i(\omega_H, \text{or } \omega_L)|$ suitable for CV charging of an EV battery. Operating just above the frequency ω_H can provide ZVS of the MOSFET main switches. Thus, operating at and above ω_H is usually preferred over operating near ω_L at LIV output of the SSIPT converter [26], [27].

C. Efficiency and Control

It is commonly believed that the SSIPT converter should operate at resonance frequency ω_S, which is the LIC operating point, for best converter efficiency at rated load [7], [10], [17]–[19], [22]. However, a more detailed study has revealed that the SSIPT converter operating at ω_H can be more efficient than the converter operating at ω_S at light loads, while the converter operating at ω_H is less efficient than the converter operating at ω_S at rated and heavy loads [11]. This feature will facilitate our implementation (C5) of a single-topology IPT charger complying with the battery charging profile described in Section III. The efficiencies η_P of the primary side and η_S of the secondary side are calculated as

$$\eta_P = \frac{\Re(Z_r)}{R_P + \Re(Z_r)} \tag{10}$$

$$\eta_S = \frac{R_L}{R_S + R_L} \tag{11}$$

where $\Re(Z_r)$ is the real component of Z_r shown in Table II. The overall efficiency of the SSIPT is given by

$$\eta = \eta_P \eta_S = \frac{\frac{\omega^2 k^2 L_P L_S (R_S+R_L)}{(R_S+R_L)^2 + X_S^2}}{R_P + \frac{\omega^2 k^2 L_P L_S (R_S+R_L)}{(R_S+R_L)^2 + X_S^2}} \frac{R_L}{R_S + R_L}. \tag{12}$$

In general, resistances R_P and R_S of the primary windings and the secondary windings are frequency dependent. The resistances are normally represented as quality factors in resonant circuits as follows:

$$Q_P(\omega) = \frac{\omega L_P}{R_P(\omega)} \tag{13}$$

$$Q_S(\omega) = \frac{\omega L_S}{R_S(\omega)} \tag{14}$$

$$Q_L = \frac{\omega_S L_S}{R_L} \tag{15}$$

where Q_L is the quality factor of a series compensated circuit with an equivalent loading resistance R_L.

As an illustration, the efficiencies versus load quality factor for $\mu = 1$, operating frequencies $\omega = \omega_P$ (CC mode) and

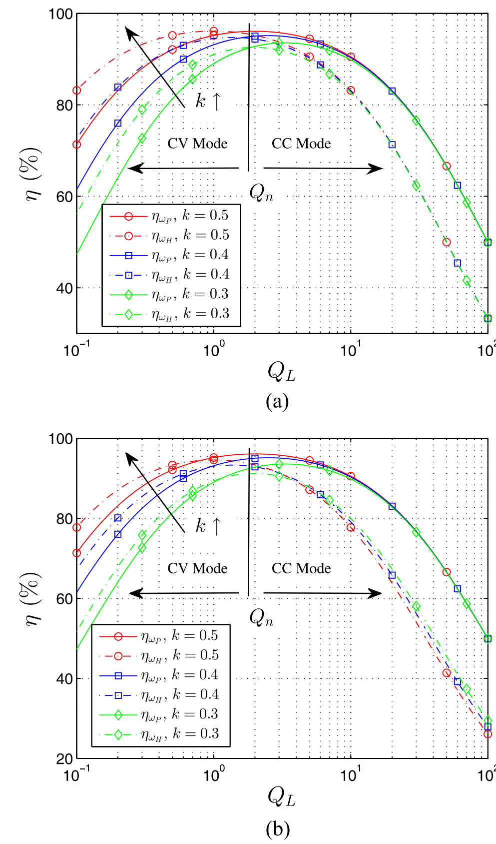

Fig. 3. Comparison of efficiency η versus Q_L operating at ω_S (CC mode) and ω_H (CV mode) for various k by using the model of (a) constant IPT transformer winding resistance and (b) constant IPT transformer winding quality factor.

$\omega = \omega_H$ (CV mode) are calculated using (12), as shown in Fig. 3. In the calculation, we use $Q_{P\,\max} = Q_{S\,\max} = Q_P = Q_S = 100$ and $k = 0.3$, 0.4, and 0.5. Fig. 3 shows that the peak efficiency in the CC operation appears at a higher Q_L than that of the CV operation. This trend supports the implementation case (C5) of battery charging described in Section III. Hence, the location of Q_L has practical importance for the peak efficiency and deserves further analysis.

For constant R_P and R_S, the maximum efficiencies $\eta_{\max_R}(\omega_P)$ and $\eta_{\max_R}(\omega_H)$ with $\mu = 1$ can be calculated using (12), and the corresponding load quality factors can be approximated as

$$Q_{L_{\mathrm{CC}_R}} \approx \frac{1}{k}, \quad \text{for } Q_P, Q_S \gg 1 \tag{16}$$

$$Q_{L_{\mathrm{CV}_R}} \approx \frac{1}{k}\sqrt{\frac{1-k}{1+\frac{Q_P}{Q_S}}}, \quad \text{for } Q_S \gg 1. \tag{17}$$

Likewise, for constant Q_P and Q_S, we have

$$Q_{L_{\mathrm{CC}_Q}} \approx \frac{1}{k}, \quad \text{for } Q_{P\,\max}, Q_{S\,\max} \gg 1 \tag{18}$$

$$Q_{L_{\mathrm{CV}_Q}} \approx \frac{1}{k}\sqrt{\frac{1-k}{1+\frac{Q_{P\,\max}}{Q_{S\,\max}}}}, \quad \text{for } Q_{S\,\max} \gg 1. \tag{19}$$

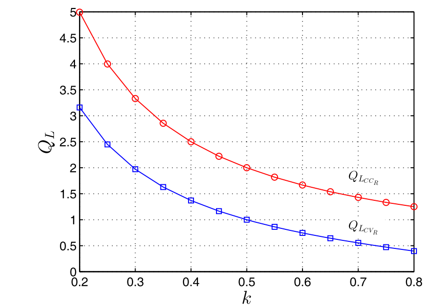

Fig. 4. Comparison of Q_L versus k at peak efficiency operating at ω_S (CC mode) and ω_H (CV mode). Both models of constant IPT transformer winding resistance and constant IPT transformer winding quality factor give near identical result.

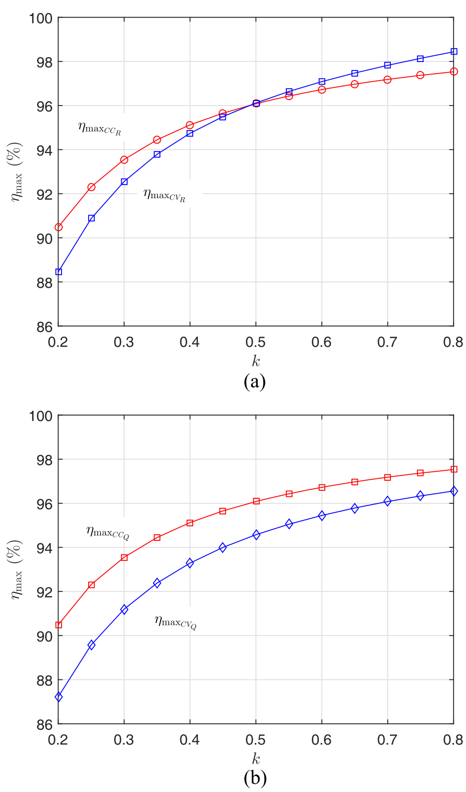

Fig. 5. Comparison of $\eta_{\max}$ versus k operating at ω_S (CC mode) and ω_H (CV mode) using model of (a) constant IPT transformer winding resistance and (b) constant IPT transformer winding quality factor.

Using (16)–(19), plots of Q_L and $\eta_{\max}$ versus k at peak efficiency can be obtained, as shown in Figs. 4 and 5. The Q_L of the battery is high during CC charging, while it is low during CV charging. Therefore, the system efficiency for implementation case (C5) will follow the solid curve during the CC mode of charging and the dashed curve during the CV mode of charging, as shown in Fig. 3. In Section III-A, the location Q_n where the system switches from CC mode to CV mode will be chosen for optimizing the overall efficiency of the EV battery charging profile.

In Section II-E, μ will be designed smaller than 1 to facilitate ZVS of MOSFET switches during CC mode of operation. In previous study [23], $\mu < 1$ has been reported to improve efficiency

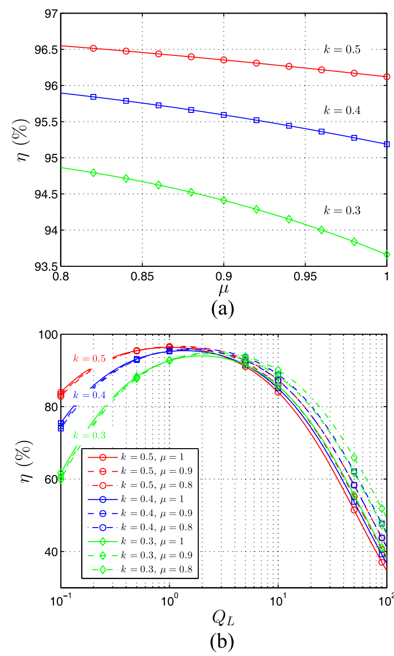

Fig. 6. Efficiency comparison of SSIPT converter operating at ω_H (CV mode). (a) Peak efficiency versus μ. (b) Efficiency versus Q_L.

of an SSIPT converter in CV mode where the maximum efficiency increases with decreasing μ, as shown in Fig. 6(a). Moreover, Fig. 6(b) shows the efficiency versus Q_L. When $Q_L > 2$, the efficiency improves with decreasing μ, and when $Q_L < 2$, the efficiency degrades slightly with decreasing μ. The overall degradation of efficiency for $\mu < 1$ in the CV mode for the normal load range is thus insignificant. The efficiency trend of the converter designed with $\mu < 1$ for the CC mode is plotted in Fig. 7(a). The efficiency degrades significantly with decreasing μ. The degradation of peak efficiency versus μ is shown in Fig. 7(b). Therefore, in our design, μ will be restricted to a few percent below 1 to facilitate soft switching during CC mode of operation.

D. Practical Transconductance and Voltage Transfer Ratio

The operating frequencies for ideal load-independent transconductance G and voltage transfer ratio E are studied in Section II-B by assuming zero power loss. As the converter is of high power efficiency, operating at the frequencies found in Section II-B will still be subject to small variations of G and E due to load variation. The practical load-independent transconductance $G(\omega_P)$ can be found by substituting ω_P into (1). The normalized error Δg is defined as

$$\begin{aligned}\Delta g &= \frac{|G_i(\omega_P)| - |G(\omega_P)|}{|G_i(\omega_P)|} \\ &= 1 - \left| \frac{\mu^2 k^2}{j\frac{\mu^2-1}{Q_P} + \frac{\mu^2}{Q_P Q_S} + \frac{\mu}{Q_P Q_L} + \mu^2 k^2} \right| \end{aligned} \tag{20}$$

which can be simplified by putting $\mu \approx 1$, i.e.,

$$\Delta g(Q_L) \approx \frac{1}{1 + k^2 Q_P Q_L}, \quad \text{for } Q_S \gg Q_L. \tag{21}$$

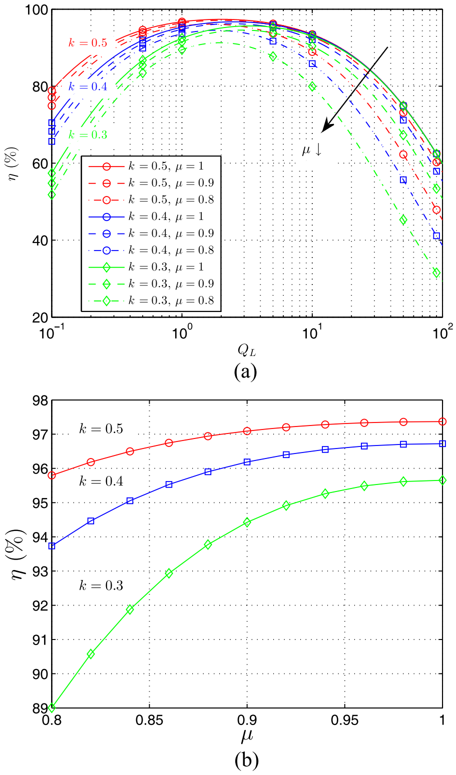

Fig. 7. Efficiency comparison of SSIPT converter operating at ω_P (CC mode). (a) Efficiency versus Q_L. (b) Peak efficiency versus μ.

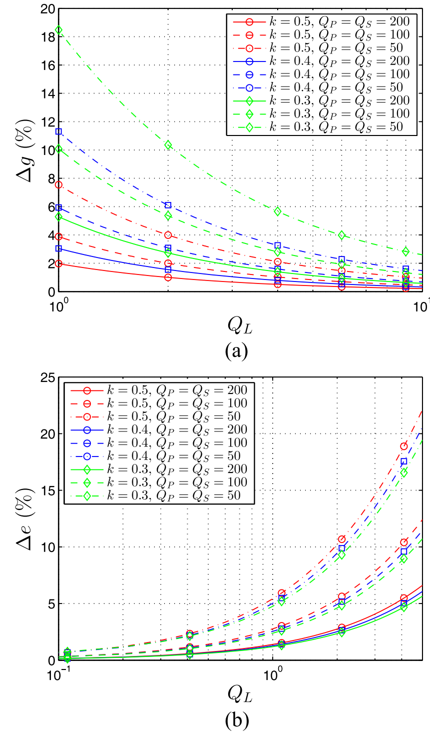

Fig. 8. Plots of (a) Δg and (b) Δe versus Q_L.

The practical LIV transfer ratio $E(\omega_H)$ can be found by substituting ω_H into (2). The normalized error $\Delta e(\omega_H)$ can be defined as

$$\Delta e = \frac{|E_i(\omega_H)| - |E(\omega_H)|}{|E_i(\omega_H)|} = 1 - \left|\frac{E_1}{E_2 - E_3}\right| \tag{22}$$

where

$$\nu = \frac{\omega_H}{\omega_S} \tag{23}$$

$$E_1 = \left(-\frac{\nu^2}{\mu^2} + 1\right)\left[-\nu^2 + 1 + \frac{j\nu}{Q_L}\right] - E_3 \tag{24}$$

$$E_2 = \left(-\frac{\nu^2}{\mu^2} + 1 + j\frac{\nu^2}{\mu^2 Q_P}\right) E_4 \tag{25}$$

$$E_3 = \frac{\nu^4}{\mu^2} k^2 \tag{26}$$

$$E_4 = -\nu^2 + 1 + j\nu\left(\frac{\nu}{Q_S} + \frac{1}{Q_L}\right). \tag{27}$$

From (20) and (22), Δg increases with decreasing Q_L while Δe increases with increasing Q_L, i.e., $G(\omega_P)$ and $E(\omega_H)$ decrease with increasing load. For illustration, Fig. 8(a) shows the percentage error on Δg and Δe versus Q_L. The load quality factor Q_{LCC_R} or Q_{LCC_Q} to achieve maximum efficiency at a particular k in CC mode is shown in Fig. 4. The value of Q_L read from Fig. 4 can be used to estimate the errors of Δg and Δe using Fig. 8. The input voltage variation of the prototype IPT converter described in Section IV can thus be designed to be within a few percent, permitting soft switching by using phase shift PWM control to regulate the desired output current and voltage of the IPT converter.

E. Input Phase Angle and Soft Switching

Inductive input phase angle is important for the MOSFET main switches to achieve zero voltage turn-on. The input impedance of the equivalent circuit model shown in Fig. 2 with parameters in Table II is given by

$$Z_{\text{in}} = Z_P + Z_r. \tag{28}$$

The corresponding input phase angle is given by

$$\theta_{\text{in}} = \tan^{-1}\left(\frac{\Re(Z_{\text{in}})}{\Im(Z_{\text{in}})}\right). \tag{29}$$

To achieve zero voltage turn-on of MOSFET switches, inductive input impedance is expected for both CC and CV modes of operation. For the CC mode, the input phase angle is given by

$$\theta_{CC} = \tan^{-1}\frac{-k^2\left(1 - \frac{1}{\mu^2}\right)}{\frac{1}{Q_P}\left[A_1^2 + \left(1 - \frac{1}{\mu^2}\right)^2\right] + k^2 A_1} \tag{30}$$

$$= \tan^{-1}\left\{Q_L\left(\frac{1}{\mu} - \mu\right)\right\}, \text{ for } Q_P \approx Q_S \gg Q_L \tag{31}$$

where $A_1 = \left(\frac{1}{Q_S} + \frac{1}{\mu Q_L}\right)$. Fig. 9(a) shows the input phase angle θ_{CC} versus Q_L in CC mode. When $\mu = 1$, θ_{CC} is exactly zero, which leaves no room for PWM control with soft switching. When μ is designed to be slightly smaller than 1, positive input phase angle can be achieved to have PWM control with soft switching.

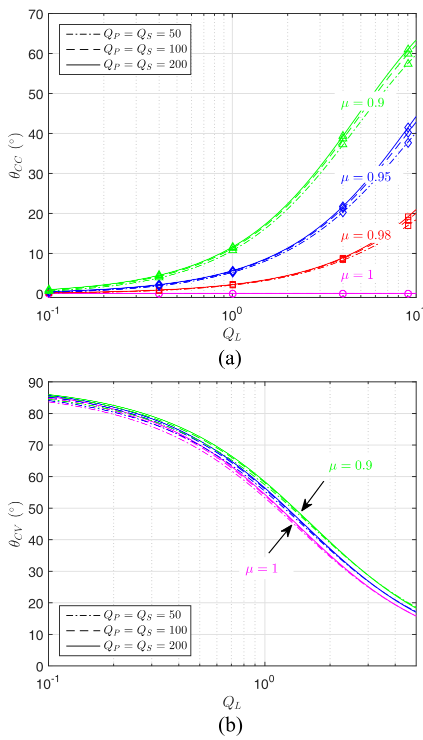

Fig. 9. Input phase angle versus Q_L for (a) CC mode and (b) CV mode of operation.

For the CV mode, the input phase angle is given by

$$\theta_{\rm CV} = \tan^{-1} \frac{\left(\frac{v^2}{\mu^2} - 1\right)\left[A_2^2 + A_3^2\right] - \frac{v^2}{\mu^2}k^2 A_3}{\frac{v^2}{\mu^2 Q_P}\left[A_2^2 + A_3^2\right] + \frac{v^2}{\mu^2}k^2 A_2} \tag{32}$$

where $A_2 = (\frac{1}{Q_S} + \frac{1}{vQ_L})$ and $A_3 = (1 - \frac{1}{v^2})$. Fig. 9(b) shows the input phase angle $\theta_{\rm CV}$ versus Q_L in CV mode, where the positive input phase angle guarantees PWM control with soft switching.

F. Control Scheme

The main circuit of the SSIPT system for EV battery charging with a control scheme is illustrated in Fig. 10. The dc voltage $U_{\rm IN}$ is modulated as a high-frequency ac voltage $v_{\rm in}$ by the set of H-bridge power MOSFET switches that drive the transmitting coil through a series compensation network. Since battery charging is a slow process for the converter, the battery can be modeled as a resistor $R_{\rm battery}$, which indicates the amount of power acquired from the charger and varies slowly according to the battery charging profile. It should be noted that $R_{\rm battery}$ has no relation to the battery internal resistance, which decreases with increasing state of charge of the battery. The rectifier with the battery can be modeled as an equivalent resistor R_L, i.e.,

$$R_L = \frac{8}{\pi^2} R_{\rm battery}. \tag{33}$$

The system will operate at ω_P, which is slightly lower than ω_S, to provide a CC and at ω_H to provide a CV. Since errors are inevitable in the output current and voltage, the input voltage is regulated by an H-bridge inverter using a phase-shift PWM control. The fundamental component of $v_{\rm in}$ is modeled as

$$v_{\rm in} = \frac{4}{\pi} U_{\rm IN} \cos\frac{\theta}{2} \quad \text{or} \quad v_{\rm in} = \frac{4}{\pi} U_{\rm IN} D \tag{34}$$

where $U_{\rm IN}$ is the dc input volatge, $\theta \in (0, \pi)$ is the phase shift angle of the H-bridge, and $D = \cos\theta/2 \in [0, 1]$ is the equivalent duty cycle. The driving signals are generated by a DSP controller. Information of the charging voltage and current in the secondary side is collected and transmitted wirelessly to the controller at the primary side.

TABLE III
CHARGING PARAMETERS

Time (h) [point in Fig. 11]	Current (A)	Voltage (V)
0 [a]	y C	$3x$
0.125 [b]	y C	$3.725x$
0.375 [c]	y C	$4x$
0.625 [d]	y C	$4x$
0.875 [e]	y C	$4.2x$
1.25 [f]	$0.6y$ C	$4.2x$
1.75 [g]	$0.27y$ C	$4.2x$
2.25 [h]	$0.133y$ C	$4.2x$
2.75 [i]	$0.05y$ C	$4.2x$

III. Design Considerations

A. Maximizing Efficiency

Suppose a battery pack consists of y parallel-connected batteries, and each battery consists of x series-connected cells [28]. The nominal values of voltage, current, and resistance of a battery pack are given by

$$U_n = 4.2 \times V \tag{35}$$

$$I_n = y\text{C A} \tag{36}$$

$$R_n = \frac{U_n}{I_n} = \frac{4.2x}{y\text{C}}\Omega \tag{37}$$

where I_n is the current at CC charging, U_n is the voltage at CV charging, R_n is the dc nominal resistance at the point of switch over from CC to CV charging, and C is the maximum current the battery can supply for 1 h. Depending on the values of x and y, different battery packs have different specifications.

For simplicity of calculating the averaged charging efficiency, the battery charging profile is approximated by several piecewise-linear segments, as shown in Fig. 11(a). From the charging parameters given in Table III, the equivalent dc resistance (Ω) of the battery $R_{\rm battery}$ ranges from $0.714R_n$ to $20R_n$, i.e., from $\frac{3x}{y\text{C}}$ to $\frac{4.2x}{0.05y\text{C}}$, as shown in Fig. 11(b). We define the load quality factor at the point of switch-over from CC to CV charging as Q_n, which is $\frac{\omega_S L_S}{\frac{8}{\pi^2}R_n}$ according to (15), (33), and (37), and this gives a charging profile ranging from $0.05Q_n$ to $1.4Q_n$, as shown in Fig. 11(b).

The equivalent resistance of the battery varies with time within the whole charging profile. Therefore, the charging efficiency varies with time. From Figs. 3 and 11(b), the choice of Q_n affects the charging efficiency versus time as shown in

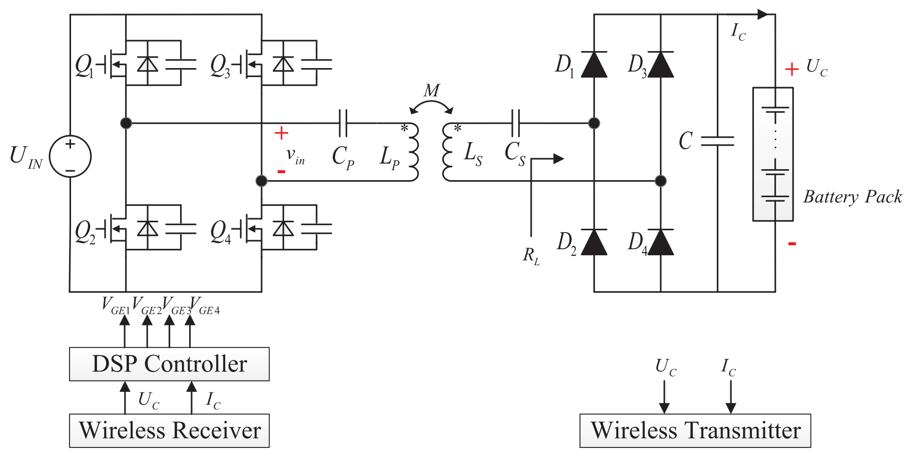

Fig. 10. Main circuit and control scheme.

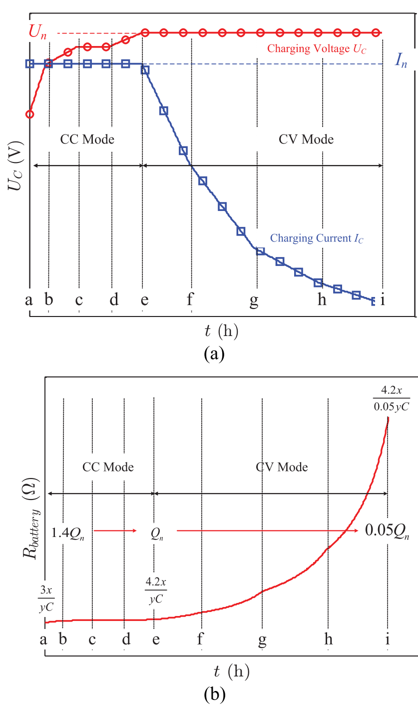

Fig. 11. (a) Piecewise-linear battery charging profile. (b) Piecewise-linear resistance of the battery during the whole charging profile.

Fig. 12. The optimization of the converter efficiency for the whole charging profile is thus simplified to choosing Q_n (or $\omega_S L_S$ since R_n is fixed) that maximizes the charging efficiency for the charging profile, i.e.,

$$\eta_{\text{overall}} = \frac{\text{outputenergy}}{\text{inputenergy}} = \frac{\int_0^T U_C(t) I_C(t) dt}{\int_0^{T_1} \frac{U_C(t) I_C(t)}{\eta_{\text{CC}}(Q_L(t))} dt + \int_{T_1}^{T} \frac{U_C(t) I_C(t)}{\eta_{\text{CV}}(Q_L(t))} dt} \tag{38}$$

where T_1 is the CC charging time, T is the total charging time, and $Q_L(T_1) = Q_n$.

We have done extensive numerical calculations to obtain an optimum $Q_{n,o}$ that corresponds to $\eta_{\text{overall}}(Q_{n,o}) =$

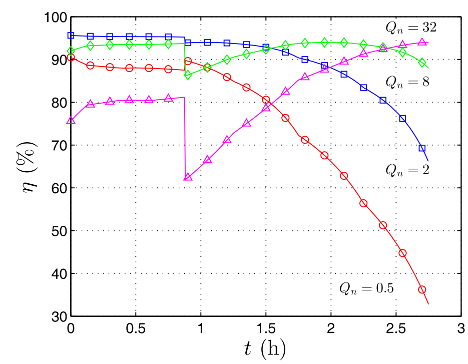

Fig. 12. Charging efficiency η profile for different values of Q_n. Overall efficiency should be maximum at a particular Q_n denoted as $Q_{n,o}$.

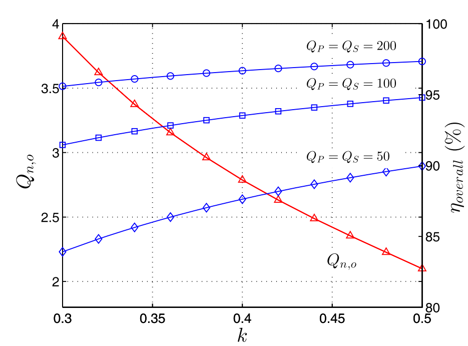

Fig. 13. Design plot of $Q_{n,o}$ versus k (red), and corresponding $\max(\eta_{\text{overall}})$ (blue), showing that $\max(\eta_{\text{overall}})$ increases with increasing k, Q_P, and/or Q_S.

$\max(\eta_{\text{overall}})$. Interestingly, there is no observable change in $Q_{n,o}$ for a range of Q_P and Q_S from 10 to 5000. Therefore, it is safe to omit Q_P and Q_S in obtaining $Q_{n,o}$. To facilitate the design, Fig. 13 presents $Q_{n,o}$ versus k graphically. In Fig. 13, the red curve plots $Q_{n,o}$ versus k, showing that $Q_{n,o}$ is not a function of Q_P or Q_S. Moreover, when comparing $Q_{n,o}$ with Q_{LCC}'s in (16) and (18), $Q_{n,o}$ is a bit higher than $\frac{1}{k}$ for all values of k. The blue curves show $\max(\eta_{\text{overall}})$ versus k for different values of $Q_P = Q_S$. From Fig. 13, a higher overall

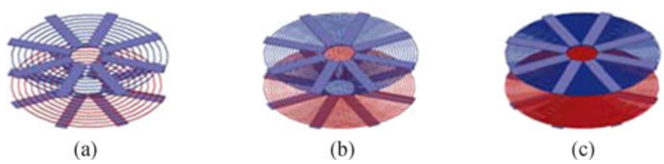

Fig. 14. Circular unipolar coupled transformer with constant inner and outer radii and evenly distributed wire distance for (a) $N = 10$, (b) $N = 20$, and (c) $N = 40$.

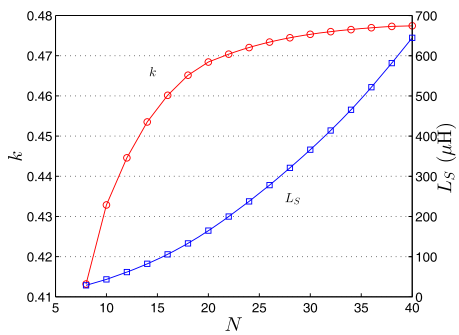

Fig. 15. Coupling coefficient k and inductance L_S (or L_P) versus number of turns N.

efficiency can be achieved by using a transformer with higher k, Q_P and/or Q_S.

B. Loosely Coupled Transformer

The loosely coupled transformer for stationary EV charging can be designed with a circular pad, a double-D pad, a double-D quadrature pad, or a bipolar pad [29], [30]. The popular primary and secondary circular pad structures shown in Fig. 14 will be adopted. In this paper, the circular pads of equal size have an outer diameter of d_o, inner diameter of d_i, and a separation gap of h. For a given structure, a higher k can be achieved with a larger $\frac{d_o}{h}$ and/or a larger ferrite section area [29]. According to the overall charging efficiency indicated in Fig. 13, using a larger pad diameter and/or better magnetic and/or conducting material, a higher $\eta_{\text{overall}}(Q_{n,o})$ can be achieved.

In Fig. 14, the simplified pad has two layers. The top layer contains the coil that generates magnetic field and the second layer contains the ferrite to reduce the reluctance. The two pads are arranged with a magnetic linking path h. It is assumed that the secondary pad is attached to the underside of an EV, while the primary pad is buried under the ground. Once an EV has stopped over the charging system, power is transferred across the air gap via magnetic coupling from the primary pad to the secondary pad.

The structure and the dimension of the loosely coupled transformer are usually designed according to some expected ranges of k, L_P, and L_S. We have performed Ansoft Maxwell simulations using the transformer structures shown in Fig. 14 with $d_o = 500$ mm, $d_i = 100$ mm, $h = 100$ mm, and the number of turns $N = N_P = N_S$ of the coils varying from 5 to 40. Design curves shown in Fig. 15 show how k and L_S vary with N, which are consistent with the results shown in [31].

C. Converter Design

Given an input voltage U_{IN}, the converter as shown in Fig. 10 provides the required charging current I_n and voltage U_n according to (35), (36), and the battery profile shown in Fig. 11. Here, Q_L varies from $1.4Q_n$ to Q_n during CC mode of charging and from Q_n to $0.05Q_n$ during CV mode of charging. Therefore, the design should satisfy (5) and (7), which are practically equivalent to

$$\begin{aligned}\frac{\pi^2 I_n}{8D_i(Q_L)U_{\text{IN}}} &= |G_i(\omega_P)|\left(1-\Delta g(Q_L)\right)\\ &= \frac{1-\Delta g(Q_L)}{\omega_P k\sqrt{L_P L_S}}\end{aligned} \tag{39}$$

$$\begin{aligned}\frac{U_n}{D_v(Q_L)U_{\text{IN}}} &= |E_i(\omega_H)|\left(1-\Delta e(Q_L)\right)\\ &= \Delta_H\left(1-\Delta e(Q_L)\right)\sqrt{\frac{L_S}{L_P}}\end{aligned} \tag{40}$$

where $\Delta_H = \left|\frac{k(\mu^2+1+\Delta)}{(2k^2-1)\mu^2+1+\Delta}\right|$ is a function of k and μ only and duty cycles D_i and D_v varying with Q_L are given in (34) for operation with LIC and LIV outputs, respectively. At rated power $Q_L = Q_n$, which corresponds to switching of CC mode to CV mode, both (39) and (40) should be satisfied, giving

$$Q_n = \frac{\pi^2}{8}\frac{I_n}{U_n}\sqrt{\frac{L_S}{C_S}} \tag{41}$$

$$= \frac{1}{k\mu}\frac{D_i(Q_n)}{D_v(Q_n)}\left(\frac{1-\Delta g(Q_n)}{\Delta_H\left(1-\Delta e(Q_n)\right)}\right) \tag{42}$$

where Q_n should be designed close to $Q_{n,o}$, as obtained from (38) for the maximum overall charging efficiency (see Fig. 13). As $R_n = \frac{U_n}{I_n}$ in (41) is fixed for a given battery, the converter can be designed with a suitable value of $\frac{L_S}{C_S}$ for achieving $Q_n = Q_{n,o}$. According to the simulated results shown in Fig. 13, $\max(\eta_{\text{overall}})$ increases with k at a reducing rate (saturates as k becomes large), and from Fig. 15, k also increases with L_S at a reducing rate. Hence, increasing L_S will offer diminishing return of $\max(\eta_{\text{overall}})$. We may therefore use $X = \frac{\Delta k}{\Delta N} = 0.001$ as an indicator for choosing an initial value of N or L_S. Other indicators may also be adopted for design [29], [30]. The value of $\omega_S = \frac{1}{\sqrt{L_S C_S}}$ obtained in (41) should be verified as being within the efficient operating range of the magnetics, switches, etc. Otherwise, a better choice of N or L_S should be used.

Duty cycles $D_i(Q_n)$ and $D_v(Q_n)$ at rated power loaded by Q_n should be designed close to 1 for best efficiency. For the reasons analyzed in Section II, the LIC operating point has a much tighter tolerance than the LIV operating point for soft switching implementation. Therefore, $D_i(Q_n)$ should be given

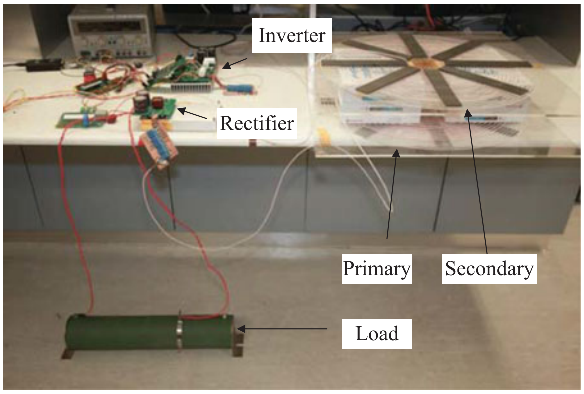

Fig. 16. Experimental prototype of the IPT system.

priority and set as 1. Thus, from (39) and (40), we have

$$\frac{I_n}{U_{\rm IN}} = \frac{8}{\pi^2}\frac{1-\Delta g(Q_n)}{\omega_P k\sqrt{L_P L_S}} \tag{43}$$

$$\frac{U_n}{U_{\rm IN}} = D_v(Q_n)\Delta_H\big(1-\Delta e(Q_n)\big)\sqrt{\frac{L_S}{L_P}}. \tag{44}$$

The values of duty cycles $D_i(1.4Q_n)$ at the beginning of the CC charging mode and $D_v(0.05Q_n)$ at the end of the CV charging mode are thus given by

$$D_i(1.4Q_n) = \frac{1-\Delta g(Q_n)}{1-\Delta g(1.4Q_n)} \tag{45}$$

$$D_v(0.05Q_n) = D_v(Q_n)\frac{1-\Delta e(Q_n)}{1-\Delta e(0.05Q_n)}. \tag{46}$$

According to Fig. 7(b), the implementation of soft switching by using $\mu < 1$ in CC mode comes with an efficiency penalty, as studied in Section II-C. In practice, μ can be assigned as 0.96. Using (30), $\theta_{\rm CC}(Q_n, \mu)$ and $\theta_{\rm CC}(1.4Q_n, \mu)$ can be obtained which should be larger than $2\cos^{-1}\{D_i(Q_n)\}$ and $2\cos^{-1}\{D_i(1.4Q_n)\}$, respectively. Otherwise, a smaller μ should be assigned with additional efficiency penalty. Thus, soft switching during CC mode of charging is guaranteed. Using (32), $\theta_{\rm CV}(Q_n)$ and $\theta_{\rm CV}(0.05Q_n)$ can be obtained, which should be larger than $2\cos^{-1}\{D_v(Q_n)\}$ and $2\cos^{-1}\{D_v(0.05Q_n)\}$ respectively. Thus, soft switching during CV mode can also be guaranteed. A more detailed illustration will be given in Section IV.

IV. Experimental Evaluation

A. Experiment

Two prototypes of an 1.5-kW IPT system with and without soft switching during CC mode of operation for EV battery charging, as shown in Fig. 16, are built with design specifications given in Table IV. Switching devices used are Infineon CoolMOS IPW60R199CP with $R_{\rm on} = 0.041\ \Omega$. Rectifier devices are STMicroelectronics STTH60AC06C with $V_F = 0.8$ V at rated power. The loosely coupled transformer is constructed according to Section III-B using Litz wire AWG38 with $N_P : N_S = 20 : 20$. The calculated and measured transformer parameters are shown in Table V. The measured parameters will be used for the subsequent design. The winding resistances are measured near the calculated operating frequencies. i.e., $R_{P_\omega} = 293$ mΩ and $R_{S_\omega} = 298$ mΩ at $f_P = \frac{\omega_P}{2\pi}$, and $R_{P_\omega} = 379$ mΩ and $R_{S_\omega} = 378$ mΩ at $f_H = \frac{\omega_H}{2\pi}$. These give the winding quality factors of approximately 174 at 50 kHz and 185 at 68.5 kHz. The equivalent resistance R_P for the model can be obtained as $R_P = R_{P_\omega} + 2R_{\rm on}$ [23], which gives $Q_P = 136$ at $f_P = 50$ kHz and 152 at $f_H = 68.5$ kHz. In contrast, Q_S is determined by the windings resistance only. Moreover, the loss due to the rectifier diodes can be modeled as a voltage source of $2V_F$ connected in series with the battery. Essentially, the quality factors of this transformer stay between the models of constant resistance and constant quality factor described in Section II-C. With the parameters k, Q_P, and Q_S measured, $Q_{L_{\rm CC}}$ can be obtained from (16) or (18), and $Q_{L_{\rm CV}}$ can be obtained from (17) or (19).

TABLE IV
Design Specification

Name	Parameter	Value
Input voltage	$U_{\rm IN}$	≈190 V
Nominal charging voltage	U_n	175 V
Nominal charging current	I_n	6.4 A
Air gap distance	h	100 mm
Transformer outer diameter	d_o	500 mm

TABLE V
Comparison of Calculated and Measured Transformer and Circuit Parameters

Transformer coupler	equal size circular pads			
Outer diameter	$d_o = 50$ cm			
Inner diameter	$d_i = 10$ cm			
Gap separation	$h = 10$ cm			
Parameter	Calculated		Measured	
k	0.468		0.447	
N_P	20		20	
N_S	20		20	
L_P	163 μH		163.46 μH	
L_S	163 μH		161.96 μH	
μ	0.96	1	0.96	1
$Q_{n,o}$	2.4	2.4	2.43	1
C_P	63.48 nF	58.50 nF	61.70 nF	61.70 nF
C_S	59.04 nF	59.04 nF	57.56 nF	61.96 nF
f_P	49.41 kHz	51.47 kHz	50.11 kHz	50.11 kHz
f_H	67.88 kHz	69.21 kHz	70.09 kHz	68.79 kHz
Parameter	Calculated		Measured	
μ	0.96	1	0.96	
$\Delta g(Q_{n,o})$	0.0159	0.0153	0.0157	
$\Delta e(Q_{n,o})$	0.0381	0.0409	0.0386	
$D_i(Q_{n,o})$	1	1	1	
$D_v(Q_{n,o})$	1	0.9570	1	
$U_{\rm in,min}$	191.66 V	191.54 V	186.5825	
$\Delta g(1.4Q_{n,o})$	0.0115	0.0110	0.0113	
$D_i(1.4Q_{n,o})$	0.9955	0.9957	0.9956	
$2\cos^{-1}\{D_i(Q_{n,o})\}$	0°	0°	0°	
$2\cos^{-1}\{D_i(1.4Q_{n,o})\}$	10.8640°	10.6477°	10.7883°	
$\theta_{CC}(Q_{n,o})$	10.7700°	0°	10.5200°	
$\theta_{CC}(1.4Q_{n,o})$	14.8975°	0°	14.5536°	
$\Delta e(0.05Q_{n,o})$	0.0021	0.0023	0.0021	
$D_v(0.05Q_{n,o})$	0.9640	0.9613	0.9634	
$2\cos^{-1}\{D_v(Q_{n,o})\}$	0°	33.7273°	0°	
$2\cos^{-1}\{D_v(0.05Q_{n,o})\}$	30.8603°	31.9918°	31.0901°	
$\theta_{CV}(Q_{n,o})$	36.2488°	34.3081°	35.8358°	
$\theta_{CV}(0.05Q_{n,o})$	85.2603°	84.9369°	85.2000°	

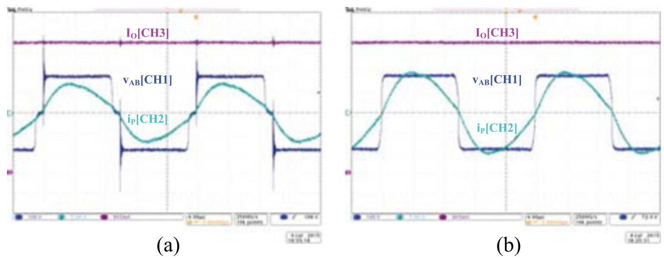

(a) (b)

Fig. 17. Waveforms of v_{AB}, i_P, and I_O at (a) start and (b) end of CC charging mode of the IPT converter designed with $\mu = 1$.

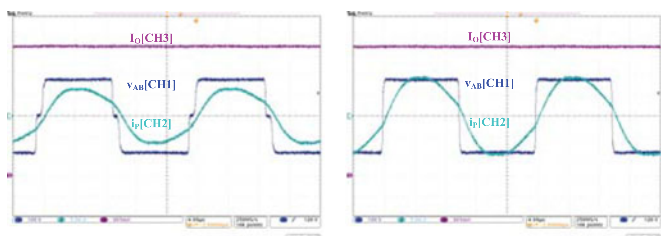

(a) (b)

Fig. 18. Waveforms of v_{AB}, i_P, and I_O at (a) start and (b) end of CC charging mode of the IPT converter designed with $\mu = 0.96$.

Two prototype converters are designed with $\mu = 0.96$ and 1. Since the physical transformers have $k = 0.447$, $Q_{n,o}$ can be read from Fig. 13 as 2.4. From (41), C_S is calculated as 59.04 nF for the two converters. Compensation capacitors C_S and C_P are measured. Their values are shown in Table V. Using Δg and Δe determined from (20) and (22), $D_i(Q_{n,o})$ can be assigned as 1 and $D_v(Q_{n,o})$ can be obtained as shown in Table V according to (42).

The rated output voltage U_n and current I_n can be scaled up or down with a suitable value of $U_{\rm IN}$ by using (21), (22) and (43), (44). The value of $U_{\rm in,min}$ can be uniquely determined in this design. However, if (43) and (44) give two significantly distinct values of $U_{\rm in,min}$ for CC and CV charging, the design should be reiterated with some appropriated values of L_P and L_S.

Using (30), inequality $\theta_{CC} > 2\cos^{-1}\{D_i(Q_n)\}$ is checked for Q_n varying from $Q_{n,o}$ to $1.4Q_{n,o}$. Hence, soft switching during LIC operation is guaranteed for the converter designed with $\mu = 0.96$. Using (32), inequality $\theta_{\rm CV} > 2\cos^{-1}\{D_v\}$ is verified for Q_n varying from $0.005Q_{n,o}$ to $Q_{n,o}$. Hence, soft switching during LIV operation is also guaranteed for the converter designed with $\mu = 0.96$. The values calculated are shown in Table V, where it is observed that the converter with $\mu = 1$ does not have soft switching during LIC output operation.

B. Soft Switching in LIC Operation for CC Charging

Using the prototype IPT converter designed with $\mu = 1$, waveforms of the converter at the start and end of the CC charging stage are shown in Fig. 17(a) and (b), respectively. It can be observed that soft switching is still achievable in Fig. 17(b), but Fig. 17(a) shows hard switching. Moreover, with $\mu = 0.96$, corresponding waveforms are shown inFig. 18(a) and (b), which clearly show ZVS operation.

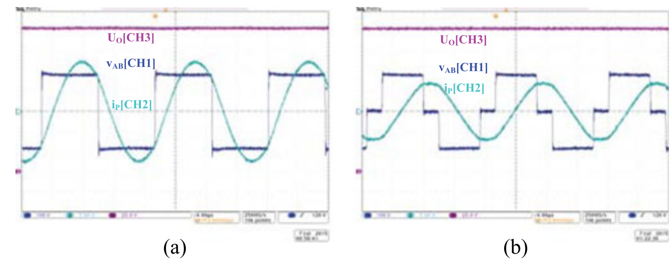

(a) (b)

Fig. 19. Waveforms of v_{AB}, i_P, and I_O at (a) start and (b) end of CV mode of charging of the IPT converter designed with $\mu = 1$.

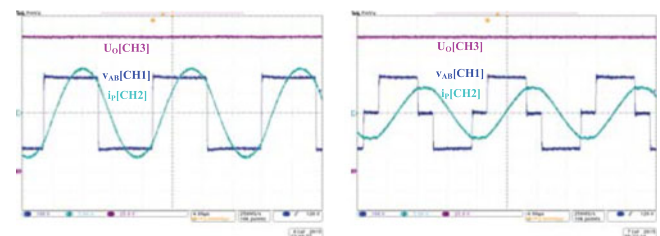

(a) (b)

Fig. 20. Waveforms of v_{AB}, i_P, and I_O at (a) start and (b) end of CV mode of charging of the IPT converter designed with $\mu = 0.96$.

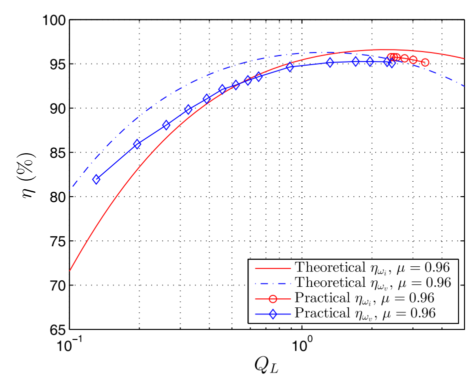

Fig. 21. Measured charging efficiency η versus load quality factor Q_L.

C. Soft Switching in LIV Operation for CV Charging

Using the prototype IPT converter designed with $\mu = 1$, waveforms of the converter at the start and end of the CC charging stage are shown in Fig. 19(a) and (b), respectively. Also, for $\mu = 0.96$, corresponding waveforms are shown in Fig. 20(a) and (b). All waveforms of LIV operation show ZVS.

D. Efficiency

A comparison of the calculated and measured efficiencies of the converter with $\mu = 0.96$ for the load quality factor varying from 0.11 to 3.08 of the battery charging profile is shown in Fig. 21. The efficiencies have been measured using a two-channel Voltech PM100 power analyzer, one channel for the dc input power and the other channel for the dc output power. Theoretical calculations are shown in solid curve for CC

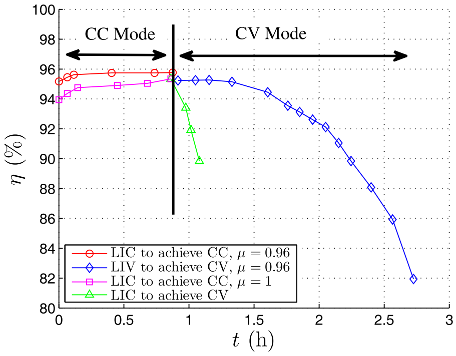

Fig. 22. Measured charging efficiency η versus time t.

output and dashed curve for CV output. Practical measurements are marked with "○" for CC mode and with "◇" for CV mode. The reasons for the practical efficiency being lower than the theoretical efficiency for both LIC and LIV operations are the following.

1) Turn-on switching loss is not completely eliminated after employing ZVS.
2) Turn-off switching loss is not considered in the model.
3) The output rectifying diode-bridge has nonlinearity, which cannot be fully represented by a single loading resistor R_L.
4) The model only considers the fundamental frequency component and omits all other components.
5) The rectifying diodes have forward voltage V_F varying with the load, which has not been considered in the loss calculation.

The experimental charging efficiency versus time of the two prototype converters is shown in Fig. 22. The converter with $\mu = 0.96$ achieving ZVS gives a higher charging efficiency (marked with "○"), while the hard switching converter with $\mu = 1$ gives lower charging efficiency (marked with "□") in CC charging mode. When the LIC output converter is controlled to operate in CV mode, the measured efficiency (marked with "△") decreases rapidly due to the required fast decrease of duty cycle at lighter load conditions and the converter ends up with hard switching. In Fig. 22, only four hard switching "△" data points are shown for the LIC operation providing a constant output voltage. The measured efficiency points (marked with "◇") are the same data points appeared in Fig. 21. There is no observable change in measured efficiency of the LIV output for the two prototype converters.

The losses in hard switching can be analyzed in terms of the typical square voltage waveform v_{in} after modulation and the current waveform i_P of the H-bridge inverter, as shown in Fig. 23(a). The switching loss and diode reverse recovery loss during switching are estimated assuming a phase angle of $\frac{\theta}{2}$. Power losses included in the calculation are switching loss P_{Switch}, diode reverse recovery loss P_{RR}, conduction loss P_{Cond}, primary winding loss P_P, secondary winding loss P_S, and forward voltage drop loss P_F of the rectifier diodes [32]. The power efficiency is thus estimated as $\eta = \frac{P_O}{P_O + P_{\text{Switch}} + P_{\text{Cond}} + P_{\text{RR}} + P_P + P_S + P_F}$. A comparison of the calculated and previously measured efficiency of the prototype

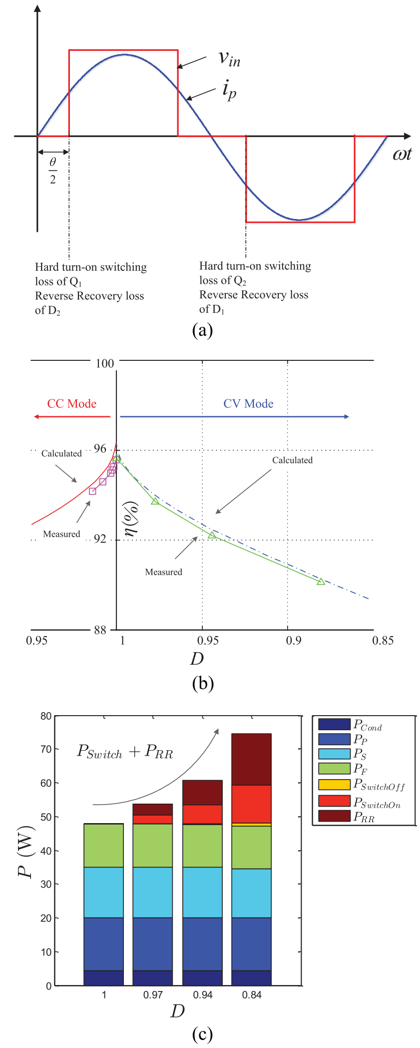

Fig. 23. Loss component estimation. (a) Illustrative voltage and current waveforms at the two phase legs of the H-bridge. (b) Measured charging efficiency η versus duty cycle D with LIC operation with $\mu = 1$. The LIC output is regulated by varying D to provide the required constant output current for CC mode and the required constant output voltage for CV mode. (c) Estimated loss components versus D, where $P_{\text{Switch}} = P_{\text{SwitchOn}} + P_{\text{SwitchOff}}$.

converter with $\mu = 1$ is given in Fig. 23(b). Since the duty cycles required for CV output by using the LIC operating point are well below the ZVS limit of $D = 0.995$ for the prototype converter with $\mu = 0.96$, a converter with a much smaller μ than 0.96 is needed to achieve soft switching. Fig. 23(c) shows the loss components versus D, which verifies that the additional losses, i.e., $P_{\text{SW}} + P_{\text{RR}}$, due to hard switching increases significantly with decreasing D. In contrary, the efficiency gained from soft switching is unable to counteract the extra loss incurred by using a much smaller μ, as explained in Section II-C. Hence, the converter operating with LIC output has a narrow range of control by using PWM modulation and is unsuitable for use as a CV output converter.

As a final remark, the converter operating efficiently with LIC output has a tight modulation margin which is only good for achieving soft switching against load variation. This supports the view that implementation cases (C2) and (C4) of battery charg-

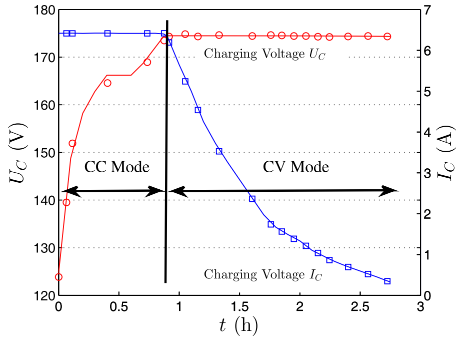

Fig. 24. Measured charging profiles of voltage U_C and current I_C.

ing cannot achieve high efficiency, as described in Section II. Fortunately, the charging current needs not be precise [15], and thus, as long as the current rating of the battery has been taken care of, the converter can be left uncontrolled at its maximum duty cycle. If a precise output current is needed against input voltage variation, a fixed-frequency ON–OFF control can be utilized for this converter [33]. Finally, the experimental charging voltage and charging current versus time for the ZVS converter with $\mu = 0.96$ are shown in Fig. 24. The overall experimental charging efficiency is found to be 94.5%.

V. Conclusion

An IPT EV charging system, which is based on a single compensated topology and two fixed operating frequencies, has been described in this paper. The S-S capacitor compensation topology has the characteristics of LIC output and LIV output at two different operating frequencies, which are suitable for CC charging and CV charging of the EV battery, respectively. Analysis and design for efficiency optimization have been studied in depth, and experimental evaluation of a 1.5-kW IPT EV battery charger has been reported.

References

[1] J. G. Hayes, M. G. Egan, J. M. D. Murphy, S. E. Schulz, and J. T. Hall, “Wide-load-range resonant converter supplying the SAE J-1773 electric vehicle inductive charging interface,” *IEEE Trans. Ind. Appl.*, vol. 35, no. 4, pp. 884–895, Jul. 1999.

[2] C. S. Wang, O. H. Stielau, and G. A. Covic, “Design considerations for a contactless electric vehicle battery charger,” *IEEE Trans. Ind. Electron.*, vol. 52, no. 5, pp. 1308–1314, Oct. 2005.

[3] G. A. Covic, J. T. Boys, M. L. G. Kissin, and H. G. Lu, “A three-phase inductive power transfer system for roadway-powered vehicles,” *IEEE Trans. Ind. Electron.*, vol. 54, no. 6, pp. 3370–3378, Dec. 2007.

[4] U. K. Madawala and D. J. Thrimawithana, “A bidirectional inductive power interface for electric vehicles in V2G systems,” *IEEE Trans. Ind. Electron.*, vol. 58, no. 10, pp. 4789–4796, Oct. 2011.

[5] H. Sakamoto, K. Harada, S. Washimiya, K. Takehara, Y. Matsuo, and F. Nakao, “Large air-gap coupler for inductive charger [for electric vehicles],” *IEEE Trans. Magn.*, vol. 35, no. 5, pp. 3526–3528, Sep. 1999.

[6] C. Duan, C. Jiang, A. Taylor, and K. Bai, “Design of a zero-voltage-switching large-air-gap wireless charger with low electrical stress for plugin hybrid electric vehicles,” in *Proc., IEEE Transp. Electrific. Conf. Expo.*, Jun. 2013, pp. 1–5.

[7] J. Sallan, J. L. Villa, A. Llombart, and J. F. Sanz, “Optimal design of ICPT systems applied to electric vehicle battery charge,” *IEEE Trans. Ind. Electron.*, vol. 56, no. 6, pp. 2140–2149, Jun. 2009.

[8] A. J. Moradewicz and M. P. Kazmierkowski, “Contactless energy transfer system with FPGA-controlled resonant converter,” *IEEE Trans. Ind. Electron.*, vol. 57, no. 9, pp. 3181–3190, Sep. 2010.

[9] S. Valtchev, B. Borges, K. Brandisky, and J. Klaassens, “Resonant contactless energy transfer with improved efficiency,” *IEEE Trans. Power Electron.*, vol. 24, no. 3, pp. 685–699, Mar. 2009.

[10] J. Shin *et al.*, “Design and implementation of shaped magnetic-resonance-based wireless power transfer system for roadway-powered moving electric vehicles,” *IEEE Trans. Ind. Electron.*, vol. 61, no. 3, pp. 1179–1192, Mar. 2014.

[11] W. Zhang, S.-C. Wong, C. K. Tse, and Q. Chen, “Analysis and comparison of secondary series- and parallel-compensated inductive power transfer systems operating for optimal efficiency and load-independent voltage-transfer ratio,” *IEEE Trans. Power Electron.*, vol. 29, no. 6, pp. 2979–2990, Jun. 2014.

[12] W. Zhang, S.-C. Wong, C. K. Tse, and Q. Chen, “Load-independent duality of current and voltage outputs of a series or parallel compensated inductive power transfer converter with optimized efficiency,” *IEEE J. Emerg. Sel. Topics Power Electron.*, vol. 3, no. 1, pp. 137–146, Mar. 2015.

[13] A. Khaligh and Z. Li, “Battery, ultracapacitor, fuel cell, and hybrid energy storage systems for electric, hybrid electric, fuel cell, and plug-in hybrid electric vehicles: State of the art,” *IEEE Trans. Veh. Technol.*, vol. 59, no. 6, pp. 2806–2814, Jul. 2010.

[14] J. Deng, S. Li, S. Hu, C. C. Mi, and R. Ma, “Design methodology of LLC resonant converters for electric vehicle battery chargers,” *IEEE Trans. Veh. Technol.*, vol. 63, no. 4, pp. 1581–1592, May 2014.

[15] H. J. Bergveld, W. S. Kruijt, and P. H. Notten, “Battery charging algorithms,” in *Battery Management Systems*. New York, NY, USA: Springer, 2002, pp. 169–192.

[16] M. K. Kazimierczuk and D. Czarkowski, *Resonant Power Converters*. Hoboken, NJ, USA: Wiley, 2011.

[17] M. Fu, H. Yin, X. Zhu, and C. Ma, “Analysis and tracking of optimal load in wireless power transfer systems,” *IEEE Trans. Power Electron.*, vol. 30, no. 7, pp. 3952–3963, Jul. 2015.

[18] R. Bosshard, J. W. Kolar, J. Muehlethaler, I. Stevanovic, B. Wunsch, and F. Canales, “Modeling and η-α-pareto optimization of inductive power transfer coils for electric vehicles,” *IEEE J. Emerg. Sel. Topics Power Electron.*, vol. 3, no. 1, pp. 50–64, Mar. 2015.

[19] W. X. Zhong and S. Y. R. Hui, “Maximum energy efficiency tracking for wireless power transfer systems,” *IEEE Trans. Power Electron.*, vol. 30, no. 7, pp. 4025–4034, Jul. 2015.

[20] X. Qu, H. Han, S.-C. Wong, C. K. Tse, and W. Chen, “Hybrid IPT topologies with constant-current or constant-voltage output for battery charging applications,” *IEEE Trans. Power Electron.*, vol. 30, no. 11, pp. 6239–6337, Nov. 2015.

[21] C. Zheng *et al.*, “High-efficiency contactless power transfer system for electric vehicle battery charging application,” *IEEE J. Emerg. Sel. Topics Power Electron.*, vol. 3, no. 1, pp. 65–74, Mar. 2015.

[22] H. Li, J. Li, K. Wang, W. Chen, and X. Yang, “A maximum efficiency point tracking control scheme for wireless power transfer systems using magnetic resonant coupling,” *IEEE Trans. Power Electron.*, vol. 30, no. 7, pp. 3998–4008, Jul. 2015.

[23] W. Zhang, S.-C. Wong, C. Tse, and Q. Chen, “Design for efficiency optimization and voltage controllability of series–series compensated inductive power transfer systems,” *IEEE Trans. Power Electron.*, vol. 29, no. 1, pp. 191–200, Jan. 2014.

[24] C. S. Wang, G. A. Covic, and O. H. Stielau, “Power transfer capability and bifurcation phenomena of loosely coupled inductive power transfer systems,” *IEEE Trans. Ind. Electron.*, vol. 51, no. 1, pp. 148–157, Feb. 2004.

[25] S. Li and C. C. Mi, “Wireless power transfer for electric vehicle applications,” *IEEE J. Emerg. Sel. Topics Power Electron.*, vol. 3, no. 1, pp. 4–17, Mar. 2015.

[26] G. B. Joung and B. H. Cho, “An energy transmission system for an artificial heart using leakage inductance compensation of transcutaneous transformers,” *IEEE Trans. Power Electron.*, vol. 13, no. 6, pp. 1013–1022, Nov. 1998.

[27] Q. Chen, S. C. Wong, C. K. Tse, and X. Ruan, “Analysis, design and control of a transcutaneous power regulator for artificial hearts,” *IEEE Trans. Biomed. Circuits Syst.*, vol. 3, no. 1, pp. 23–31, Feb. 2009.

[28] A. Affanni, A. Bellini, G. Franceschini, P. Guglielmi, and C. Tassoni, “Battery choice and management for new-generation electric vehicles,” *IEEE Trans. Ind. Electron.*, vol. 52, no. 5, pp. 1343–1349, Oct. 2005.

[29] M. Budhia, G. A. Covic, and J. T. Boys, “Design and optimization of circular magnetic structures for lumped inductive power transfer systems,” *IEEE Trans. Power Electron.*, vol. 26, no. 11, pp. 3096–3108, Nov. 2011.

[30] A. Zaheer, H. Hao, G. Covic, and D. Kacprzak, "Investigation of multiple decoupled coil primary pad topologies in lumped IPT systems for interoperable electric vehicle charging," *IEEE Trans. Power Electron.*, vol. 30, no. 4, pp. 1937–1955, Apr. 2015.
[31] C. Fernández, O. Garcia, R. Prieto, J. Cobos, S. Gabriels, and G. Van Der Borght, "Design issues of a core-less transformer for a contact-less application," in *Proc. 17th Annu. IEEE Appl. Power Electron. Conf. Expo.*, 2002, vol. 1, pp. 339–345.
[32] J. Klein, "Synchronous buck MOSFET loss calculations with Excel model," Fairchild Semiconductor, San Jose, CA, USA, Appl. Note AN6005, 2006.
[33] Y. S. Lee and Y. C. Cheng, "Design of switching regulator with combined FM and on-off control," *IEEE Trans. Aerosp. Electron. Syst.*, vol. AES-22, no. 6, pp. 725–731, Nov. 1986.

Zhicong Huang (S'14) received the B.Sc. degree in electrical engineering and automation and M.Sc. degree in mechanical and electronic engineering from Huazhong University of Science and Technology, Wuhan, China, in 2010 and 2013, respectively. He is currently working toward the Ph.D. degree in power electronics at the Hong Kong Polytechnic University, Kowloon, Hong Kong.

His current research interests include wireless power transfer and power electronics.

Siu-Chung Wong (M'01–SM'09) received the B.Sc. degree in physics from the University of Hong Kong, Hong Kong, in 1986, the M.Phil. degree in electronics from the Chinese University of Hong Kong, Hong Kong, in 1989, and the Ph.D. degree from the University of Southampton, Southampton, U.K., in 1997.

He joined the Hong Kong Polytechnic in 1988 as an Assistant Lecturer. He is currently an Associate Professor with the Department of Electronic and Information Engineering, The Hong Kong Polytechnic University, Hong Kong, where he conducts research in power electronics. From 2012 to 2015, he was appointed as a Chutian Scholar Chair Professor by the Hubei Provincial Department of Education, China, and the appointment was hosted by Wuhan University of Science and Technology, Wuhan, China. In 2013, he was appointed as Guest Professor by the School of Electrical Engineering, Southeast University, Nanjing, China. He was a Visiting Scholar with the Center for Power Electronics Systems, Virginia Tech, Blacksburg, VA, USA, in November 2008, Aero-Power Sci-tech Center, Nanjing University of Aeronautics and Astronautics, Nanjing, in January 2009, and the School of Electrical Engineering, Southeast University, in March 2012.

Dr. Wong is a member of the Electrical College, The Institution of Engineers, Australia. He is an editor of the *Energy and Power Engineering* journal and a member of the Editorial Board of the *Journal of Electrical and Control Engineering*. He serves as a Guest Associate Editor for the IEEE JOURNAL OF EMERGING AND SELECTED TOPICS IN POWER ELECTRONICS, Special Issue on Power Electronics for Biomedical Applications, 2014. He serves as an Associate Editor for the IEEE TRANSACTIONS ON CIRCUITS AND SYSTEMS II: EXPRESS BRIEFS.

Chi K. Tse (M'90–SM'97–F'06) received the B.Eng. (Hons.) degree (with first class honors) in electrical engineering and Ph.D. degree from the University of Melbourne, Melbourne, Australia, in 1987 and 1991, respectively.

He is currently a Chair Professor with the Hong Kong Polytechnic University, Hong Kong, where he was the Head of the Department of Electronic and Information Engineering from 2005 to 2012. He is the author/coauthor of ten books, 20 book chapters, and more than 500 papers in research journals and conference proceedings and holds five U.S. patents.

Dr. Tse has received a number of research and industry awards, including Prize Paper Awards by the IEEE TRANSACTIONS ON POWER ELECTRONICS in 2001 and 2015, the Best Paper Award by the *International Journal of Circuit Theory and Applications* in 2003, *RISP Journal of Signal Processing* Best Paper Award in 2014, two Gold Medals at the International Inventions Exhibition in Geneva, Switzerland, in 2009 and 2013, and a number of recognitions by the academic and research communities, including honorary professorship by several Chinese and Australian universities, Chang Jiang Scholar Chair Professorship, IEEE Distinguished Lectureship, Distinguished Research Fellowship by the University of Calgary, Gledden Fellowship and International Distinguished Professorship-at-Large by the University of Western Australia. While with the Hong Kong Polytechnic University, he received the President's Award for Outstanding Research Performance twice, the Faculty Research Grant Achievement Award twice, the Faculty Best Researcher Award, and several teaching awards. He serves/has served as the Editor-in-Chief for the IEEE TRANSACTIONS ON CIRCUITS AND SYSTEMS II: EXPRESS BRIEFS (2016–2017), *IEEE Circuits and Systems Magazine* (2012–2015), and *IEEE Circuits and Systems Society Newsletter* (since 2007), an Associate Editor for three IEEE Journal/Transactions, an Editor for the *International Journal of Circuit Theory and Applications*, and is on the editorial boards of a few other journals.